

Low-loss strong index modulated ultra-thermally stable optical phase-change material for broadband nonvolatile photonics

Cite as: J. Appl. Phys. **133**, 053101 (2023); <https://doi.org/10.1063/5.0120033>

Submitted: 20 December 2022 • Accepted: 14 January 2023 • Published Online: 06 February 2023

Ming Li, Shubing Li, Menghan Deng, et al.



View Online



Export Citation



CrossMark

Journal of Applied Physics **Special Topics** Open for Submissions [Learn More](#)







Low-loss strong index modulated ultra-thermally stable optical phase-change material for broadband nonvolatile photonics

Cite as: J. Appl. Phys. 133, 053101 (2023); doi: 10.1063/5.0120033

Submitted: 20 December 2022 · Accepted: 14 January 2023 ·

Published Online: 6 February 2023



Ming Li,¹ Shubing Li,¹ Menghan Deng,¹ Xionghu Xu,¹ Kai Dai,¹ Anyang Cui,^{1,a)}  Xin Zhou,¹ Kai Jiang,¹ 
Liyan Shang,¹  Yawei Li,¹  Jinzhong Zhang,¹ Liangqing Zhu,¹  Junhao Chu,^{1,2} and Zhigao Hu^{1,2,b)} 

AFFILIATIONS

¹Technical Center for Multifunctional Magneto-Optical Spectroscopy (Shanghai), Department of Physics, School of Physics and Electronic Science, East China Normal University, Shanghai 200241, China

²Collaborative Innovation Center of Extreme Optics, Shanxi University, Taiyuan, Shanxi 030006, China

^{a)}Electronic mail: aycui@phy.ecnu.edu.cn

^{b)}Author to whom correspondence should be addressed: zghu@ee.ecnu.edu.cn

ABSTRACT

Optical phase change materials (O-PCMs) have attracted increasing attention and provide promising solutions for non-volatile reconfigurable photonics due to their large index contrast and non-volatile switching characteristics. In this work, we have explored the optical phase change properties of a dozen different O-PCMs and established the corresponding gene bank. Among these O-PCMs, Ge₁Sb₂Se₃Te₁ (G1S2S3T1) films exhibit unprecedented low-loss, strong light modulation capability, and ultra-thermal stability capability, which are prepared by pulsed laser deposition. Meanwhile, we investigate the phase transition kinetic mechanism of G1S2S3T1 films by transmission electron microscope, temperature dependent transmission spectroscopy, and temperature dependent Raman spectroscopy. It is found that the wide bandgap (1.09 eV) in the amorphous state, the large bandgap variation (0.51 eV) between amorphous and crystalline states, the needle-like configuration of its crystalline state, and the special phase change process contribute to strong refractive index modulation. Moreover, we find that their ultra-thermal stability is from a strong Sb–Se bond. Through the simulation, we found that G1S2S3T1 can be applied to prepare ultra-low loss waveguide devices. The present work represents a significant step in the development of broadband nonvolatile photonics derived from O-PCMs.

© 2023 Author(s). All article content, except where otherwise noted, is licensed under a Creative Commons Attribution (CC BY) license (<http://creativecommons.org/licenses/by/4.0/>). <https://doi.org/10.1063/5.0120033>

I. INTRODUCTION

Ovshinsky suggested a promising data storage technology based on phase-change materials (PCMs) in 1968,¹ which relies on the reversible transformation between the amorphous and crystalline states of PCMs by short optical or electrical pulses with very low energy (as low as femtojoules).^{2–4} The phase transformation is accompanied by a significant change in optical reflectivity ($\Delta n > 1$) and electrical resistivity between these two solid states. Currently, chalcogenide-based PCMs have already been applied in commercial optical storage media such as CDs, DVDs, and Blu-ray disks.^{5,6} At the same time, the reversible electrical resistivity contrast of PCMs can be applied in non-volatile electronic memory,

which is considered to accelerate the success of artificial synapses for the hardware acceleration of artificial neural networks (ANNs);⁷ inline phase-change radio frequency switch (IPCS)⁸ for monolithic microwave integrated circuits (MMICs);⁹ etc. Hence, PCMs are necessary to develop new nonvolatile memory technology and re-form the current nonvolatile memory applications.

Owing to the fact that current reconfigurable silicon photonic integrated circuits (PICs) primarily rely on the thermo-optic (TO)^{10–12} or electro-optic (EO)^{13,14} effect of silicon, both effects suffer from several limitations such as minimal tuning of the refractive index (usually, $\Delta n < 0.01$), a large footprint (at least a few tens of micrometers for the length of active regions), etc. Furthermore,

both types of switching mechanisms are volatile, requiring a continuous power supply (typically several milliwatts) to maintain the optical switching state.^{15,16} Therefore, devices based on O-PCMs have attracted the attention of researchers all over the world. The amorphization speed of O-PCMs can reach the sub-nanosecond time scale in picoseconds, and the crystallization speed can reach the sub-nanosecond to nanosecond time scale.² At the same time, the cycle stability can enable ultra-fast operation potentially over 10^{15} switching cycles.¹⁷ The final state of the switch can also be retained for 10 years under ambient conditions without any external power supply reference.⁴ Furthermore, O-PCMs are extremely scalable and can be scaled down to the nanometer scale.¹⁸ Therefore, O-PCM-based devices are considered the next generation of reconfigurable PICs being used for various applications including photonic switches,^{19,20} photonic memory,^{21,22} programmable gate arrays,^{12,23} optical computing,²⁴ and optical neural networks.²⁵ It is believed that the identification and understanding of the optical phase change properties unique to the O-PCMs would greatly accelerate material discovery and future applications.

For reconfigurable PICs applications, low optical loss becomes crucial due to the proximity of the optical mode to the O-PCMs in nanophotonic waveguides. Thus, the selection criterion has to be redefined to accommodate the low optical absorption and high refractive index change as required for integrated photonic applications. This is quantified by the figures of merit (FOM) $\frac{\Delta n}{k_a}$ and $\frac{\Delta n}{k_c}$, where Δn is the refractive index contrast between two states, k_a and k_c are the extinction coefficients in the amorphous and crystalline states, respectively. The FOMs are widely cited to gauge the performance of active materials used in switches and modulators. It has been determined that the FOM correlates quantitatively with insertion loss (IL) and contrast in all-optical, electro-optical, and magneto-optical devices. In this respect, several emerging O-PCMs have been proposed, which exhibit high FOMs in various technologically important wavelengths, such as the typical quantum emitter (nitrogen vacancy centers in diamond) wavelength (633 nm), the telecommunication O-band (1310 nm), and the telecommunication C-band (1550 nm).

O-PCM-based PIC devices can be operated by optical phase modulation, absorption modulation, or both. Phase modulation is suitable for Mach-Zhender Interferometers (MZIs)¹⁰ or directional coupler-based switches.¹² Absorption modulation is beneficial for cavity-based switches²⁰ and changes in both optical phase and loss result in significant extinction rates. A widely investigated chalcogenide material system in O-PCMs is the Ge-Sb-Te system, particularly, Ge₂Sb₂Te₅ (GST). GST at 1550 nm, for example,⁸ typically operates by both mechanisms owing to the simultaneous large change in the refractive index ($\Delta n \sim 2.7$) and extinction coefficient ($\Delta k \sim 1$), which is ideal for applications, such as microring switches and photonic memories. However, k_a of amorphous GST reaches up to 0.12 at 1550 nm, corresponding to 42 000 dB/cm attenuation, which is too high for most PICs applications. Hu *et al.*²⁶ and Muskens *et al.*²⁷ are also simultaneously exploring new low-loss O-PCM devices, with the former focusing on Ge₂Sb₂Se₄Te₁ and the latter on Sb₂Se₃.

In this work, we reported the optical constants of several different O-PCMs, compared them with previous studies, and found a new class of Ge-Sb-Te-Se-based O-PCM, G1S2S3T1, which had

low-loss strong index modulated performance at 1310 and 1550 nm. We revealed that it also had ultra-thermal stability. Summing up the analysis of the results, it can be seen that G1S2S3T1 had a rod-like knitting structure, van der Waals layered structure after crystallization, a wide bandgap (1.09 eV) in the amorphous state, the large bandgap variation (0.51 eV), a high crystallization temperature (~ 560 K), and the special phase change process. Moreover, these exceptional properties make G1S2S3T1 different from other O-PCMs, which is expected to have a substantial application in future PICs applications.

II. EXPERIMENT SECTION

A. Film deposition

The pulsed laser deposition (PLD) technique was used to prepare O-PCMs films in this work. A KrF excimer laser beam with a wavelength of 248 nm, and a pulse length of 20 ns was employed. The pulse energy was 4 J/cm², and the pulse repetition rate was typically set to 10 Hz. The background pressure in the PLD chamber was 7.0×10^{-7} mbar. During deposition, highly pure argon was used resulting in the pressure of 2.0×10^{-2} mbar. The silicon substrates and sapphire substrates were ultrasonic cleaned by de-ionized water and acetone. The cleaned substrates were positioned inside the chamber and paralleled with the target. The distance between the target and the substrate was 5.5 cm. Commercial targets with high-purity (99.99%) were utilized and rotated continuously in order to improve the uniformity of the phase change films. The substrate temperature was measured by a thermocouple and maintained at ~ 300 K during the deposition process. GeTe (MS) films were deposited onto Si substrates by radio frequency magnetron co-sputtering of Ge and Te targets at room temperature with a background pressure of 1.0×10^{-6} mbar. Moreover, in an attempt to acquire crystalline O-PCMs films, the as-deposited films were annealed at the corresponding temperature in the argon atmosphere to prevent oxidation. The annealing equipment used is a tube furnace (Thermcraft XST-2-0-12-1V1-E28). The crystallinity of O-PCM films was obtained by annealing at a nominal temperature of 300°C for 30 min and same conditions for both PLD and sputtered films.

B. Characterizations

The spectroscopic ellipsometry (SE) measurements were performed in the photon energy range of 400–2500 nm at an incident angle of 70° by a vertical variable-angle SE (J. A. Woollam Co., Inc.). Fitting of the real and imaginary parts of the refractive indices was performed with the Woollam WVASE software. The structural characteristics were measured by x-ray diffraction (XRD; Japan SmartLab) with Cu K α radiation from 0° to 90° and a scanning rate of 0.02°/s at room temperature. The surface morphology of samples was studied by Atomic Force Microscopy (AFM, Dimension Icon, Bruker). The chemical valence and chemical composition were acquired by XPS (Thermo ESCALAB 250Xi) equipped with Al K α x-ray source, the spectra were referenced to C 1s at 284.8 eV. The transmission electron microscopy (TEM) specimen was prepared with a dual-beam focused ion beam (FIB) system (Nanolab Helios 650) using Ga ion accelerating voltage

(30 kV). Then, ion-milling operation was implemented from 24 pA to 9.3 nA. The HRTEM images, SAED, and elemental mapping were performed by the STEM mode of a JEM Grand ARM300F microscope with double spherical aberration (Cs) correctors and an EDX detector operated at 300 kV. The transmittance of the films was recorded by a double beam UV-Vis-NIR spectrophotometer (PerkinElmer Lambda 950). Scan electron microscopy (SEM, PIONEER Two, RAI TH) was operated at 30 kV. The temperature dependent Vis-NIR transmission spectrum was obtained by a Fourier transform infrared spectrometer (Vertex 80V) and a high temperature/high pressure all-round cell (Specac HTHP GS05855). In addition, Raman spectroscopy (Jobin-Yvon LabRAM HR Evolution spectrometer) measurements were performed using a 532 nm laser in the range of $50\text{--}300\text{ cm}^{-1}$ and a THMSE 600 heating/cooling stage (Linkam Scientific Instruments).

C. Simulations

The mode profiles of optical waveguide units with rectangular cladding geometry were simulated using a finite difference Eigen (FDE) wave optics model through the numerical MODE solutions (Eigenmode Solver Analysis). All modes are TE-polarized.

III. RESULTS AND DISCUSSION

Here, we prepared several different O-PCMs by PLD and magnetron sputtering (MS) and characterized optical constants by SE. Based on these data and previous studies, we established an O-PCMs gene bank and performed a systematic O-PCMs screening. The experimental data and the fitting process of different

O-PCMs can be found in Figs. S1–S8, in the [supplementary material](#). Figure 1 illustrates optical constants of amorphous and crystalline phases of different O-PCMs films on silicon substrates from the visible range to near-infrared (400–2500 nm) by SE measurements. As shown in Table I, the optical properties of various O-PCMs are compared at 633, 1310, and 1550 nm. From the comparison of Figs. 1(b) and 1(c), it can be seen that the different deposition techniques also have a small effect on the optical constants of the films, where it is obvious that the films prepared by PLD are better than those prepared by MS. Among these O-PCMs, the one with the weakest modulation capability and ultrahigh optical loss is the Sb_2Te_3 (ST) both at 1310 and 1550 nm. By comparing the optical parameters of Sb_2Te_3 , $\text{Sb}_2\text{Se}_{0.5}\text{Te}_{2.5}$, and $\text{Sb}_2\text{Se}_{1.5}\text{Te}_{1.5}$ in Table I, it can be seen that the optical modulation capacity (Δn) is improving and the IL ($\frac{\Delta n}{k_0}$) is in progressive optimization as the amount of Se substituting Te in ST increases. However, when Te is completely substituted by Se as Sb_2Se_3 , its optical modulation ability is weakened again at the telecommunication band.

From Table I, we can notice that Sb_2S_3 is the only candidate for cavity-based, switch among the O-PCMs that supports low-loss operation with a contrasting index contrast of 0.84 at 633 nm. At 1310 nm, SbSe and G1S2S3T1 are ideal for applications such as microring switches and photonic memories. Since G1S2S3T1 has larger Δn than that of SbSe, G1S2S3T1 will have greater light modulation capabilities than SbSe. At 1550 nm, GST, $\text{Ge}_2\text{Sb}_2\text{Se}_4\text{Te}_1$, Sb_2Se_3 , Sb_2S_3 , SbSe, $\text{Sb}_2\text{Se}_{1.5}\text{Te}_{1.5}$, and G1S2S3T1 all have great potential for application to PICs. Among them, Sb_2Se_3 will be preferred for non-volatile phase-only control in near-IR silicon photonics applications as it has zero IL at both 1310 and 1550 nm and large

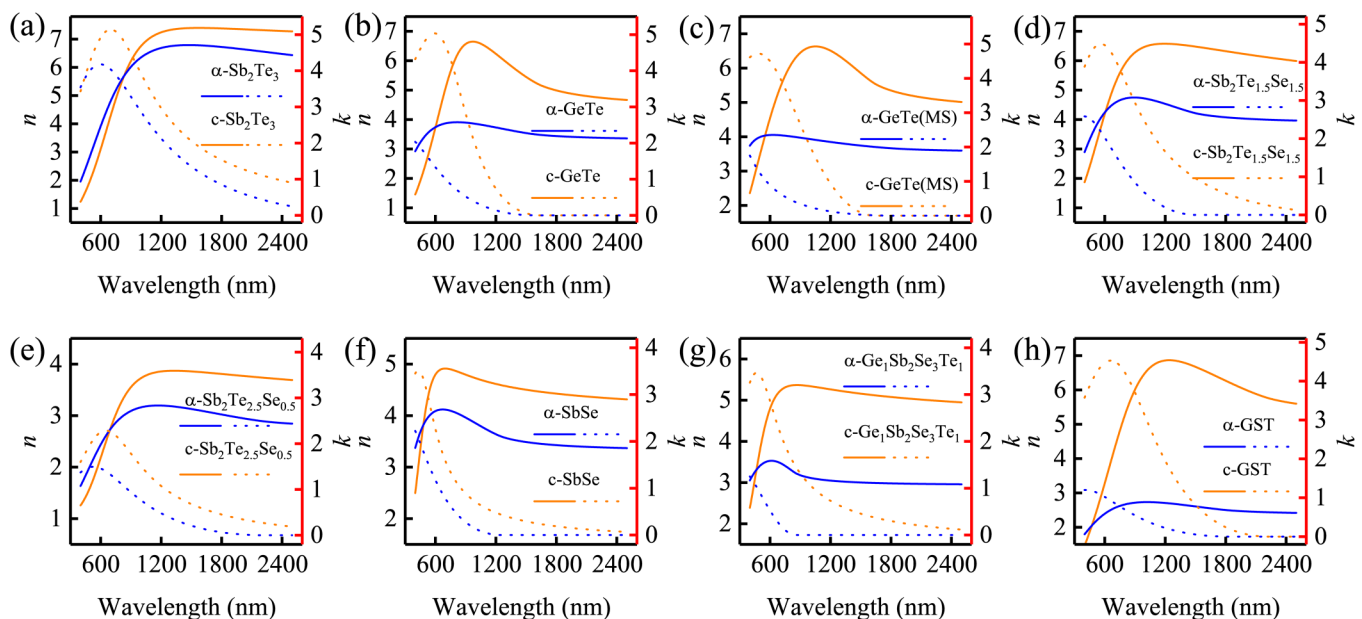


FIG. 1. (a)–(h) Optical constants of amorphous (blue lines) and crystalline (orange lines) phases of different O-PCMs films on silicon substrates from the visible range to near-infrared. The solid lines represent the refractive index n , and the dashed lines are the extinction coefficient k . The samples were deposited by PLD except for the samples with MS remarks deposited by magnetron sputtering in this work.

TABLE I. Optical constants comparison of different O-PCMs at 633, 1310, and 1550 nm, respectively.

	633 nm				1310 nm				1550 nm			
	Δn	Δk	$\frac{\Delta n}{k_c}$	$\frac{\Delta n}{k_s}$	Δn	Δk	$\frac{\Delta n}{k_c}$	$\frac{\Delta n}{k_s}$	Δn	Δk	$\frac{\Delta n}{k_c}$	$\frac{\Delta n}{k_s}$
GeTe ²²	1.15	1.5	1.28	0.48	1.86	0.42	30.16	3.9	1.83	0.24	53.94	6.79
GST ⁸	0.16	2.54	0.08	0.4	2.82	1.2	5.93	1.69	2.74	1.07	137	2.51
Ge ₂ Sb ₂ Se ₄ Te ₁ ²⁶	0.62	1.75	0.77	0.24	1.81	0.63	86.54	2.79	1.75	0.42	U.D.	4.17
Sb ₂ Se ₃ ²⁷	1.12	0.87	2.1	0.8	0.82	0.001	U.D.	820.	0.77	0	U.D.	U.D.
Sb ₂ S ₃ ²⁷	0.84	0.276	U.D.	3.04	0.58	0	U.D.	U.D.	0.6	0	U.D.	U.D.
GeTe	0.41	3.8	0.34	0.08	2.27	0.31	34.54	6.08	1.82	0.21	2267	84.68
GeTe(MS)	0.83	3.56	1.05	0.19	2.5	0.44	31.6	4.8	2.01	0.02	93.12	54.9
Sb ₂ Te ₃	0.73	0.89	0.18	0.14	0.58	0.77	0.32	0.23	0.61	0.7	0.49	0.31
GST	1.18	3.55	1.22	0.26	4.17	1.31	28.65	2.87	4.02	0.65	103.37	5.84
SbSe	0.76	0.97	0.75	0.38	1.01	0.39	U.D.	2.59	1.01	0.27	U.D.	3.74
Sb ₂ Se _{0.5} Te _{2.5}	0.17	0.86	0.12	0.07	0.69	0.54	1.91	0.77	0.74	0.46	4.21	1.17
Sb ₂ Se _{1.5} Te _{1.5}	0.2	2.49	0.11	0.05	2.15	1.28	27.34	1.59	2.27	0.88	U.D.	2.58
G1S2S3T1	1.47	2.61	3.65	0.56	2.19	0.61	U.D.	3.6	2.15	0.42	U.D.	5.12

U.D. stands for undefined as the denominator is zero. The samples were deposited by PLD except for the samples with MS remarks deposited by magnetron sputtering in this work.

Δn (~ 0.82 at 1310 nm and ~ 0.77 at 1550 nm).²⁷ Moreover, Sb₂Se_{1.5}Te_{1.5} and G1S2S3T1 have larger Δn of 2.27 and 2.15 at 1550 nm, respectively, which means stronger optical modulation capability. Combining all parameters, G1S2S3T1 is the most desirable material among these O-PCMs in the telecommunication band.

In order to determine the crystalline structure and phase information of the crystalline G1S2S3T1 film, the x-ray diffraction (XRD) measurement was implemented and shown in Fig. 2(a). The XRD characteristic diffraction peaks are located at 9.06°, 18.2°, 36.75°, 46.3°, 56.2°, can be indexed to the (003), (006), (0012), (0015),

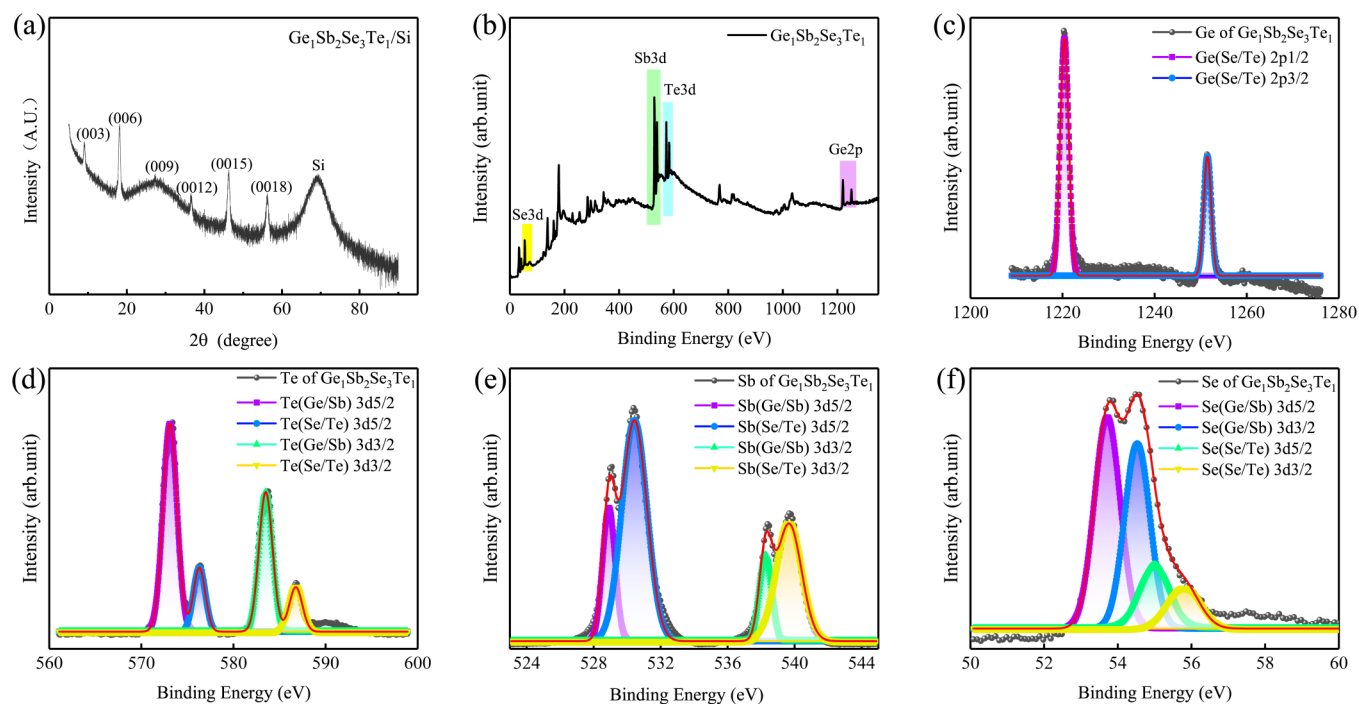


FIG. 2. (a) XRD patterns of the thermally crystallized G1S2S3T1 film on a silicon substrate. (b) The overall XPS spectra of the G1S2S3T1 film. The fitted XPS spectra of (c) Ge 2p, (d) Te 3d, (e) Sb 3d, and (f) Se 3d in the G1S2S3T1 film, respectively.

(0018) crystal faces of the hexagonal (HEX) structure. It can be inferred that the G1S2S3T1 film grows along the *c*-axis direction on the silicon substrate. Moreover, according to the strongest peak located at 18.2° and the Bragg Formula, the interplanar spacing $d_{(006)}$ of hexagonal G1S2S3T1 was calculated to be about 0.489 nm.

To investigate the valence state and surface chemical composition, the as-deposited G1S2S3T1 film have been characterized by x-ray photoelectron spectroscopy (XPS). Figure 2(b) demonstrates the overall XPS spectra of the G1S2S3T1 film, and it reveals the presence of Ge 2p, Te 3d, Sb 3d, and Se 3d without any other impurity element. As shown in Fig. 2(c), the high-resolution Ge 2p spectra can be fitted into two peaks at 1220.3 and 1251.4 eV,²⁸ which can be assigned to the lattice in the (Se/Te)-Ge framework. The high-resolution Te 3d spectrum [Fig. 2(d)] exhibits four peaks at 573.1, 576.4, 583.8, and 586.8 eV, corresponding to non-oxygenated (Ge/Sb)-Te 3d_{5/2}, (Se/Te)-Te 3d_{5/2}, (Ge/Sb)-Te 3d_{3/2}, (Se/Te)-Te 3d_{3/2}, respectively. From Fig. 2(e), (Ge/Sb)-Sb 3d_{5/2}, (Se/Te)-Sb 3d_{5/2}, (Ge/Sb)-Sb 3d_{3/2}, and (Se/Te)-Sb 3d_{3/2} peaks appeared at 528.9, 530.5, 538.3, and 539.6 eV, respectively, which was in accordance with early reports.²⁷ The de-convoluted Se 3d spectra [Fig. 2(f)], the first two fitting peaks (located at 53.7 and 54.5 eV) are corresponding to (Ge/Sb)-Se 3d_{5/2} and (Ge/Sb)-Se 3d_{3/2}.²⁹ However, the other two higher peaks with the binding energy of about 55 and 55.8 eV belong to (Se/Te)-Se band.³⁰ The atomic percentage of Ge:Sb:Se:Te was acquired by calculation to be 2.03:4.09:5.83:1.85 and the corresponding molecular formula is Ge₁Sb₂Se_{2.9}Te_{0.93}.

The as-deposited Ge₁Sb₂Se₃Te₁ film and annealed crystalline Ge₁Sb₂Se₃Te₁ film have been characterized by the Scanning Electron Microscope (SEM) and high-resolution TEM (HRTEM)

to further evaluate the morphology and microstructure shown in Figs. 3(a)–3(d). As shown in Fig. 3(a), the amorphous G1S2S3T1 film on a 40 nm titanium nitride (TiN)/Si substrate has a flat cross section similar to its surface without a visible lattice structure, which is in good agreement with the AFM image. The TiN layer is added to increase the conductivity of the substrate for HRTEM observation. The TEM image in Fig. 3(b) shows a low-magnification image of the as-deposited G1S2S3T1 film after annealing at a nominal temperature of 400°C for 30 min and a large number of holes and granular contrast can be clearly observed. As shown in Fig. 3(c), it can be clearly observed that the crystalline G1S2S3T1 has a rod-like grain interweaving morphological configuration, which is consistent with the previous rough and uneven AFM image. These interwoven crystal rods can be seen as a series of photon capture traps, which contribute to the strong index modulated ability of G1S2S3T1. Figure 3(d) shows a high-magnification image of a well-crystallized area with strong lattice contrast visible. We find that the presence of multiple contrast lines in the back-folded region are similar to back-folded layered 2D materials in Fig. 3(d).³¹ To further illustrate the crystal order, the corresponding selected area electron diffraction (SAED) is shown in the inset of Fig. 3(d), where the pattern affirms the features of hexagonal G1S2S3T1. Meanwhile, we calculated the average pitch of 4.887 nm based on the length of 10 cycles, which matches with the (006) phase of HEX G1S2S3T1 and is in good agreement with the XRD results (0.489 nm). The energy-dispersive x-ray (EDX) elemental mapping images in Figs. 3(e)–3(h) show the elemental composition and distribution. The four Ge, Sb, Se, and Te elements are evenly distributed in the entire sample, which indicates that the

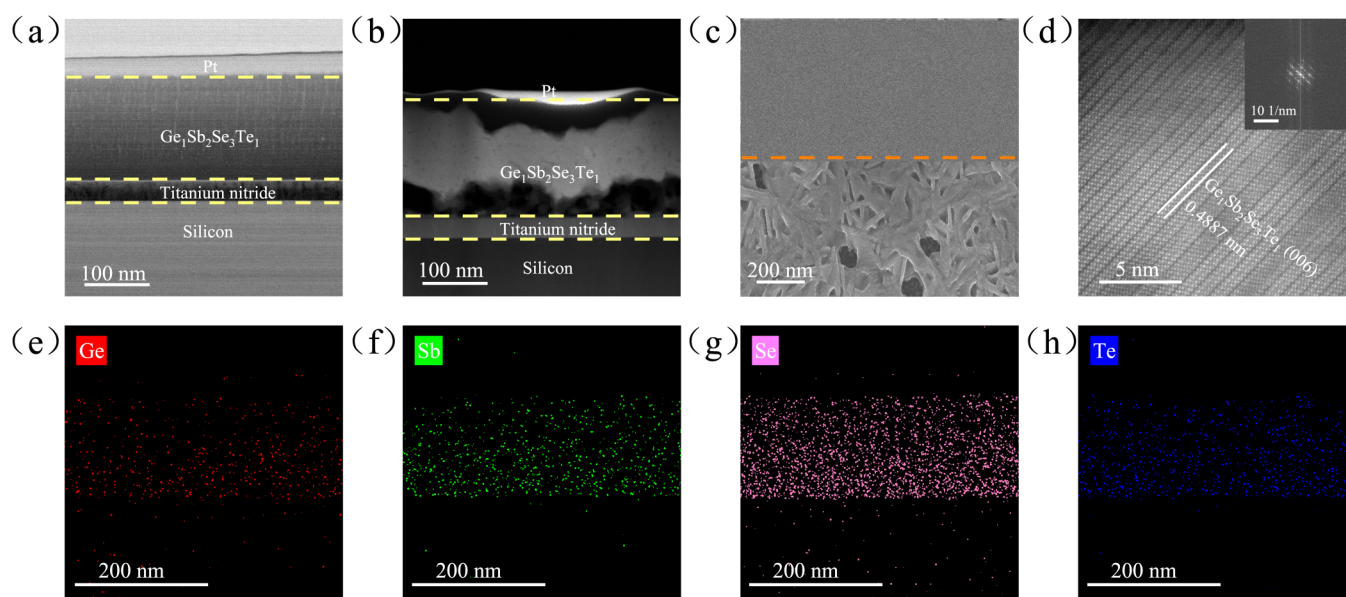


FIG. 3. (a) and (b) TEM images of as-deposited and thermally crystallized ~ 200 -nm-thick G1S2S3T1 films on a 40 nm TiN/Si substrate. (c) SEM images of the as-deposited (above the dashed line) thermally crystallized (below the dashed line) G1S2S3T1 film on a silicon substrate. (d) HRTEM images and (inset) SAED patterns of the crystalline G1S2S3T1 film. EDX elemental mapping images of the as-deposited G1S2S3T1 film of (e) Ge, (f) Sb, (g) Se, (h) Te, respectively.

G1S2S3T1 film is uniformly deposited on the substrate by PLD technology.

As shown in Fig. 4(a), to obtain the optical bandgap E_g^{opt} of amorphous and crystalline G1S2S3T1 films, ultraviolet (UV)-visible (Vis)-near-infrared (NIR) transmittance measurements were performed. The optical bandgap E_g^{opt} can be given as $\alpha = -\ln(T_{op})/d$ and $ah\nu = A(h\nu - E_g^{opt})^r$. According to indirect transitions and the Tauc-Lorentz dispersion model (the gray lines), with $r = 2$, the optical bandgap E_g^{opt} of amorphous and crystalline G1S2S3T1 films are ~ 1.09 and ~ 0.58 eV, respectively. The bandgap variation ΔE_g^{opt} is 0.51 eV, which is much larger than traditional O-PCM GST ($\Delta E_g^{opt} \sim 0.2$ eV).³² To determine the phase change temperature of the G1S2S3T1 film, the temperature dependent Vis-NIR transmission spectrum was performed in Fig. 4(b). To make the phase transition process look more intuitive, we plotted the contour map [Fig. 4(c)] derived from the data in Fig. 4(b). It is obvious from the graph that the temperature at which the color changes most significantly, i.e., the phase change temperature, is around 560 K. The phase change temperature is much higher than that of other similar O-PCMs, such as GST

(420 K)²⁸ and GSST (470 K).²⁶ The higher phase change temperature implies better thermal stability. Furthermore, the wavelength region with the greatest transmittance variation to G1S2S3T1 is near 1000 nm. When the temperature is higher than 560 K, the change in transmittance begins to diminish until no change occurs, which means that the change in optical properties occurs mainly between the amorphous phase and the metastable phase. To illustrate more clearly the future prospects of G1S2S3T1 for applications in the communication band, we have plotted the transmission-temperature diagram at the telecommunication O-band (1310 nm) and the telecommunication C-band (1550 nm). As shown in Fig. 4(d), the G1S2S3T1 film has better performance at 1310 nm than at 1550 nm, i.e., higher transparency in the amorphous state and stronger light-blocking ability in the crystalline state. Moreover, the transmittance contrasts of 1310 nm and 1550 nm are $\sim 40\%$ and $\sim 35\%$, which is obviously superior to other conventional photonic switches such as silicon-on-insulator (SOI) (0.1%)³³ and lithium niobate (LN) (0.1%).³⁴

As Raman scattering spectra are sensitive to the variations of local distortions and atomic substitution, which can be usually used to analyze the detailed structural variation of O-PCMs.

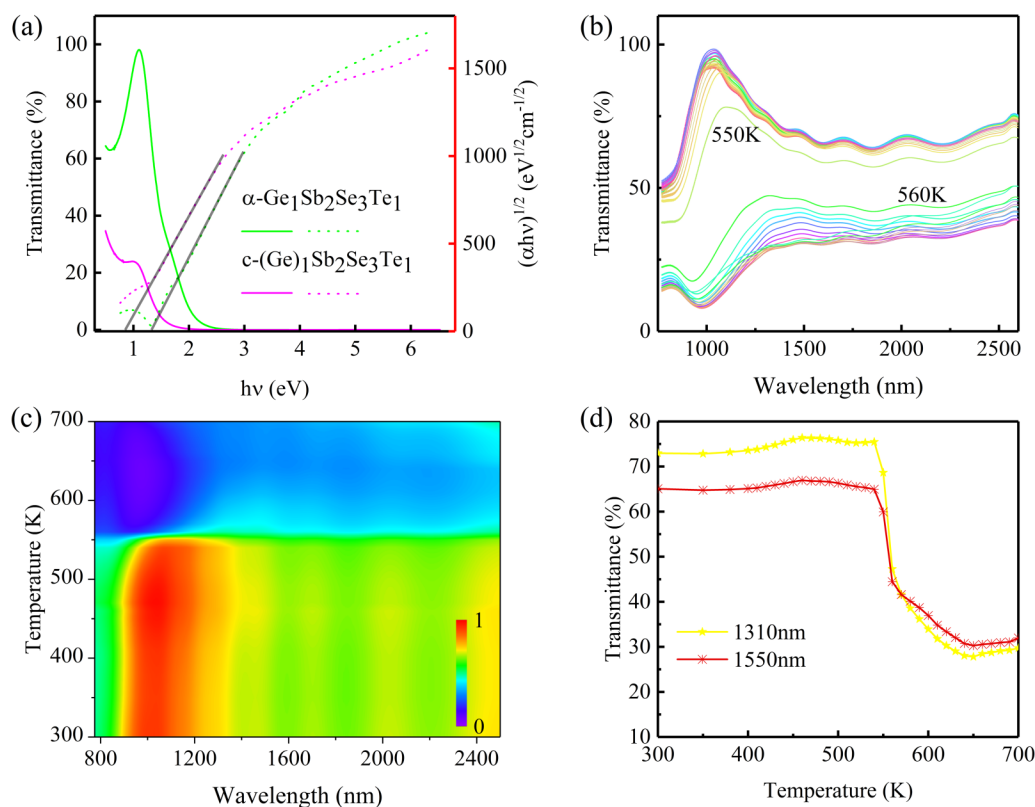


FIG. 4. (a) UV-NIR transmittance spectra of the amorphous (green lines) G1S2S3T1 film and crystalline (magenta lines) G1S2S3T1 film on a sapphire substrate. The solid lines represent the transmittance, and the dashed lines represent $(ah\nu)^{1/2}$. (b) Vis-NIR transmission spectrum for an as-deposited G1S2S3T1 film on a sapphire substrate with a heating rate of 10 K/min. (c) Transmission contour map derived from the data in the temperature dependence of the visible-NIR transmission spectrum. (d) Transmission-temperature diagram of the G1S2S3T1 film at 1310 and 1550 nm, respectively.

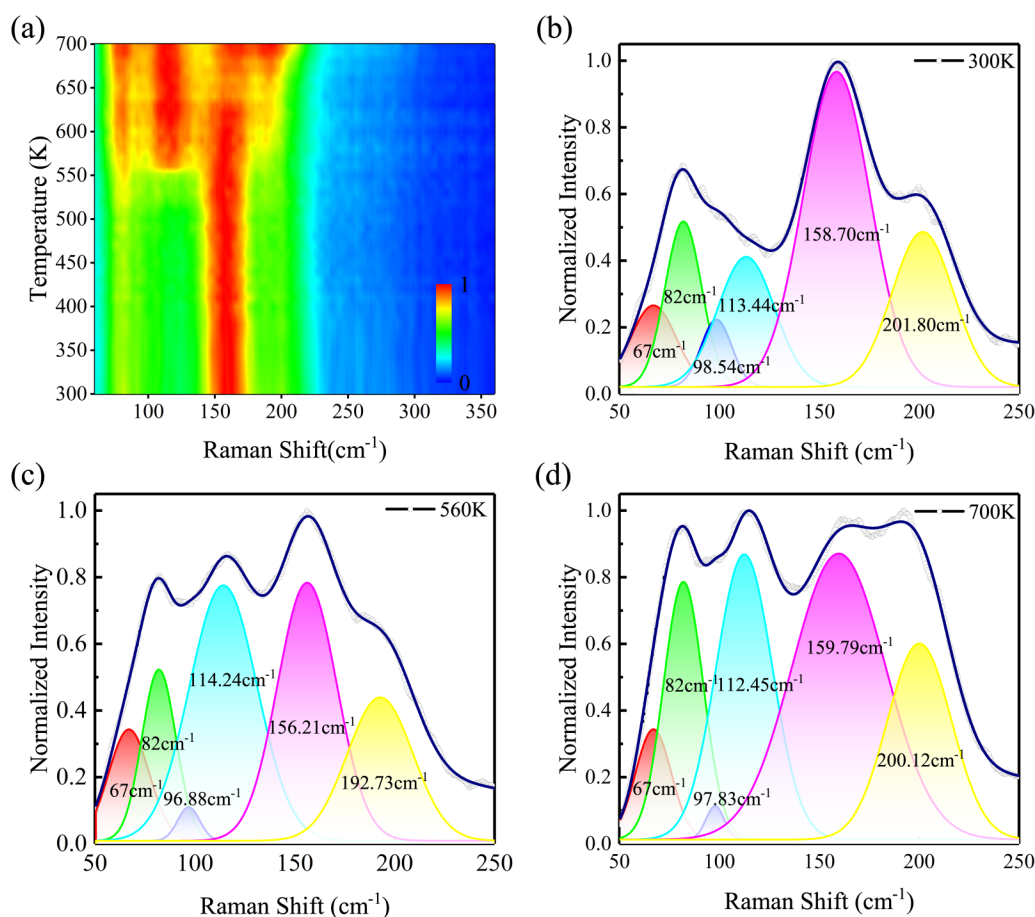


FIG. 5. Temperature dependence of Raman scattering spectra for an amorphous G1S2S3T1 film on a silicon substrate with a heating rate of 10 K/min. (a) Intensity normalized contour map redrawn with the data in temperature dependence of Raman spectra. Raman spectra of the G1S2S3T1 film at (b) 300, (c) 560, and (d) 700 K, including the fitting data to the Lorentz–Gaussian functions for each state, respectively.

To explore the structural evolution and the crystallization temperature of the G1S2S3T1 film during the phase transition, an intensity normalized contour map was redrawn with the data in temperature dependence of Raman spectra in Fig. 5(a). The phase change temperature at the point of significant intensity change is around 560 K from Fig. 5(a), which coincides with the results of the previous temperature dependent transmission spectrum analysis. To further analyze the structural variation during the phase transition, we fit the data to the Lorentz–Gaussian functions^{35–38} at 300, 560, and 700 K, respectively. In order to obtain more reliable fitting results, it is necessary to use as few fitted oscillators as possible to reduce the number of independent parameters involved in the fitting process on the basis of ensuring the fitting effect. For the Raman scattering spectra of the G1S2S3T1 film studied in this work, six Gaussian oscillators were used to fit the Raman scattering spectra, which are labeled by 1, 2, 3, 4, 5, and 6, respectively. The best fitting results of the Raman scattering spectra corresponding to the previous temperature point are used as the initial parameters of

the fitting of the spectra corresponding to the next temperature point. Table II gives the designation of each Raman phonon mode and its corresponding central frequency and relative intensity at 300, 560, and 700 K, respectively. The relatively two weak peaks vary during the amorphous-metastable transition and remain essentially unchanged during the metastable-HEX, peak 1 ($\sim 67\text{ cm}^{-1}$), and peak 3 ($\sim 96\text{--}98\text{ cm}^{-1}$), correspond to the bending vibration F_2 mode and the corner-share vibration A_1 mode of the GeTe_4 tetrahedrals, respectively. The two peaks undergo an intensity change only during the metastable-HEX, peak 2 ($\sim 82\text{ cm}^{-1}$) and peak 6 ($\sim 192\text{--}202\text{ cm}^{-1}$), which represent the vibration E_0 mode of the GeSe_4 tetrahedrals and the stretching mode of Sb–Se of Sb_2Se_3 pyramids. The peak with consistently poor intensity variation, peak 5 ($\sim 156\text{--}160\text{ cm}^{-1}$), stands for the Se–Se bending vibration modes both in GeSe_4 tetrahedral and Sb_2Se_3 pyramids. The peak continuously increases as the temperature rises. Peak 3 ($\sim 113\text{ cm}^{-1}$) represents the vibration E_g^2 mode of Sb_2Se_3 pyramids. The whole phase change process is that as the

TABLE II. Identification of each Raman phonon frequency and corresponding vibration mode of the G1S2S3T1 film at 300, 560, and 700 K, respectively. The phonon frequencies (PF) are all in units of cm^{-1} . RI is an abbreviation for relative intensity.

Vibration mode		300 K	560 K	700 K
1	PF	67	67	67
	RI	0.265	0.343	0.341
2	PF	82	82	82
	RI	0.517	0.521	0.786
3	PF	98.54	96.88	97.83
	RI	0.232	0.11	0.111
4	PF	113.44	114.24	112.45
	RI	0.411	0.776	0.869
5	PF	158.70	156.21	159.79
	RI	0.967	0.783	0.871
6	PF	201.80	192.73	200.12
	RI	0.486	0.439	0.601

temperature rises the GeTe_4 tetrahedrals are first formed into a metastable state, and then as the temperature continues to rise the Sb_2Se_3 pyramids are formed, finally, forming HEX G1S2S3T1. Based on the analysis of the above results, it is clear that the high phase transition temperature and ultra-thermally stability are derived from the strong Sb–Se bond in Sb_2Se_3 pyramids.³⁹

As shown in Fig. S10(b), in the [supplementary material](#), the silicon waveguide can support a tightly confined mode with a large effective index n_{eff} of $2.873 + 0.059i$ while the G1S2S3T1 film is at the crystalline state. Whereas the mode in Fig. S10(c), in the [supplementary material](#), spreads a moderate effective index n_{eff} of $2.668 + 1.615 \times 10^{-6}i$ while the G1S2S3T1 film is at the amorphous state. At 1550 nm, the simulated loss of the Si waveguide device is 20 914 dB/cm for the crystalline state. The Si waveguide device suffers from negligible loss (0.057 dB/cm) in the amorphous state at 1550 nm, showing promising performance for PICs applications. Figures S10(d) and S10(e), in the [supplementary material](#) illustrate that the cladding Si_3N_4 waveguide has an effective index n_{eff} of $2.033 + 0.104i$ in the crystalline state and an effective index n_{eff} of $1.70 + 2.56 \times 10^{-5}i$ in the amorphous state. At 1550 nm, the simulated loss of this waveguide device is 36 510 dB/cm for the crystalline state and 9.0125 dB/cm in the amorphous state. Based on the simulation results of Si devices and Si_3N_4 devices, the fact is that the G1S2S3T1 film can be applied to more commonly used SiO_2 -clad Si_3N_4 and SiO_2 -clad Si PICs with ultra-low ILs. We also did a simple simulation of a G1S2S3T1-based micro-ring resonator switch, and we can see that the GSST can be used to switch the optical path of the drop port via crystalline/amorphous switching from Fig. S11, in the [supplementary material](#). As shown in Table S1, in the [supplementary material](#), comparing the simulation results of waveguide devices based on different O-PCMs proves once again that the overall performance of the G1S2S3T1 is better than the others.

IV. CONCLUSION

In summary, we have investigated the optical constants of several different O-PCMs by SE and performed a systematic

O-PCMs screening by establishing the corresponding O-PCMs gene bank based on these data and previous studies. After a series of comparisons, we found a new class of O-PCM, G1S2S3T1, which has low optical absorption and strong refractive index modulation both at 1310 and 1550 nm. The phenomenon can be attributed to the bandgap (1.09 eV) in the amorphous state and the large bandgap variation (0.51 eV) between amorphous and crystalline states. The interwoven crystal rods of crystalline G1S2S3T1 can be seen as a series of photon capture traps, which also contribute to strong index modulated ability. Benefitting from the strong Sb–Se bond, G1S2S3T1 has a high phase transition temperature (560 K) and ultra-thermal stability. The simulation results of the Si waveguide and Si_3N_4 waveguide demonstrate that the G1S2S3T1 film can be applied to the fabrication of ultra-low loss PICs. These results enable a new path for applications in photonic switches, photonic memory, programmable gate arrays, optical computing, optical neural networks, and tunable metasurfaces. Moreover, the origination mechanisms of the strong refractive index modulation and ultra-thermal stability, as demonstrated in our example of G1S2S3T1, points out a generic route in the search for new O-PCMs optimized for broadband nonvolatile photonics.

SUPPLEMENTARY MATERIAL

See the [supplementary material](#) for more details about the experimental and best fitting ellipsometric spectra Ψ and Δ of amorphous and crystalline phases for different O-PCM films, a three-dimensional (3D) surface topography AFM image of amorphous and crystalline phases of the G1S2S3T1 film on a silicon substrate, a schematic of a waveguide loaded with a 25 nm SiO_2 /25 nm G1S2S3T1 cladding and the modal intensity profiles of amorphous and crystalline states in the Si waveguide and Si_3N_4 waveguide, a schematic of a waveguide loaded with a 25 nm SiO_2 /25 nm G1S2S3T1 cladding Si-ring resonator and the modal intensity profiles of amorphous and crystalline states, and the simulation results of Si waveguide and Si_3N_4 waveguide loaded with a 25 nm SiO_2 /25 nm O-PCMs cladding.

ACKNOWLEDGMENTS

This work was financially supported by the National Natural Science Foundation of China (NNSFC, Grant Nos. 62090013, 12104156, 61974043, 62074058, and 61974044), the National Key R&D Program of China (Grant No. 2019YFB2203403), the Projects of Science and Technology Commission of Shanghai Municipality (Grant Nos. 21JC1402100 and 19511120100), China Postdoctoral Science Foundation (Grant Nos. 2020TQ0099 and 2020M681222), and the Program for Professor of Special Appointment (Eastern Scholar) at Shanghai Institutions of Higher Learning and Shanghai Pujiang Program (No. 20PJ1403600).

AUTHOR DECLARATIONS

Conflict of Interest

The authors have no conflicts to disclose.

Author Contributions

Ming Li: Writing – review & editing (equal). **Shubing Li:** Data curation (supporting). **Menghan Deng:** Data curation (supporting). **Xionghu Xu:** Data curation (supporting). **Kai Dai:** Data curation (supporting). **Anyang Cui:** Data curation (equal). **Xin Zhou:** Formal analysis (supporting). **Kai Jiang:** Data curation (supporting). **Liyan Shang:** Supervision (supporting). **Jinzhong Zhang:** Supervision (supporting). **Liangqing Zhu:** Data curation (supporting); Supervision (supporting). **Junhao Chu:** Supervision (equal). **Zhigao Hu:** Writing – review & editing (equal).

DATA AVAILABILITY

The data that support the findings of this study are available from the corresponding author upon reasonable request.

REFERENCES

- ¹S. R. Ovshinsky, *Phys. Rev. Lett.* **21**, 1450 (1968).
- ²D. Loke, T. H. Lee, W. J. Wang, L. P. Shi, R. Zhao, Y. C. Yeo, T. C. Chong, and S. R. Elliott, *Science* **336**, 6088 (2012).
- ³G. I. Meijer, *Science* **319**, 1628 (2008).
- ⁴M. Wuttig and N. Yamada, *Nat. Mater.* **6**, 824 (2007).
- ⁵D. Lencer, M. Salinga, B. Grabowski, T. Hickel, J. Neugebauer, and M. Wuttig, *Nat. Mater.* **7**, 972 (2008).
- ⁶K. Ding, J. Wang, Y. Zhou, H. Tian, L. Lu, R. Mazzarello, C. L. Jia, W. Zhang, F. Rao, and E. Ma, *Science* **366**, 6462 (2019).
- ⁷N. K. Upadhyay, H. Jiang, Z. Wang, S. Asapu, Q. Xia, and J. J. Yang, *Adv. Mater. Technol.* **4**, 1800589 (2018).
- ⁸H. Lo, E. Chua, J. C. Huang, C. C. Tan, C. Y. Wen, R. Zhao, L. Shi, C. T. Chong, J. Paramesh, T. E. Schlesinger, and J. A. Bain, *IEEE Trans. Electron Devices* **57**, 312 (2010).
- ⁹N. El-Hinnawy, P. Borodulin, B. Wagner, M. R. King, J. S. Mason, E. B. Jones, S. McLaughlin, V. Veliadis, M. Snook, M. E. Sherwin, R. S. Howell, R. M. Young, and M. J. Lee, “A four-terminal, inline,” *IEEE Electron Device Lett.* **34**, 1313 (2013).
- ¹⁰Y. C. Shen, N. C. Harris, S. Skirlo, M. Prabhu, T. Baehr-Jones, M. Hochberg, X. Sun, S. J. Zhao, H. Larochelle, D. Englund, and M. Soljacic, *Nat. Photon.* **11**, 441 (2017).
- ¹¹P. Dong, W. Qian, H. Liang, R. Shafiha, N. N. Feng, D. Feng, X. Zheng, A. V. Krishnamoorthy, and M. Asghari, *Opt. Express* **18**, 9852 (2010).
- ¹²D. Pérez, I. Gasulla, L. Crudgington, D. J. Thomson, A. Z. Khokhar, K. Li, W. Cao, G. Z. Mashanovich, and J. Capmany, *Nat. Commun.* **6**, 636 (2017).
- ¹³J. Van Campenhout, W. M. J. Green, S. Assefa, and Y. A. Vlasov, *Opt. Express* **17**, 24020 (2009).
- ¹⁴C. Qiu, X. Ye, R. Soref, L. Yang, and Q. Xu, *Opt. Lett.* **37**, 3942 (2012).
- ¹⁵N. Youngblood, C. Rios, E. Gemo, J. Feldmann, Z. Cheng, A. Baldycheva, W. H. P. Pernice, C. D. Wright, and H. Bhaskaran, *Adv. Funct. Mater.* **29**, 1807571 (2019).
- ¹⁶L. H. Yu, Y. L. Yin, Y. C. Shi, D. X. Dai, and S. L. He, *Optica* **3**, 159 (2016).
- ¹⁷S. Raoux, F. Xiong, M. Wuttig, and E. Pop, *MRS Bull.* **39**, 703–710 (2014).
- ¹⁸S. Raoux, G. W. Burr, M. J. Breitwisch, C. T. Rettner, Y. C. Chen, R. M. Shelby, M. Salinga, D. Krebs, S. H. Chen, H. L. Lung, and C. H. Lam, *IBM J. Res. Dev.* **52**, 465–479 (2008).
- ¹⁹Z. R. Fang, J. J. Zheng, A. Saxena, J. Whitehead, Y. Y. Chen, and A. Majumdar, *Adv. Optical Mater.* **9**, 2002049 (2021).
- ²⁰Z. Fang, R. Chen, J. J. Zheng, and A. Majumdar, *IEEE J. Sel. Top. Quantum Electron.* **28**, 1 (2022).
- ²¹C. Rios, M. Stegmaier, P. Hosseini, D. Wang, T. Scherer, C. D. Wright, H. Bhaskaran, and W. H. P. Pernice, *Nat. Photon.* **9**, 725 (2015).
- ²²C. Rios, N. Youngblood, Z. Cheng, M. L. Gallo, W. H. P. Pernice, C. D. Wright, A. Sebastian, and H. Bhaskaran, *Sci. Adv.* **5**, 5759 (2019).
- ²³W. F. Zhang and J. P. Ya, *Nat. Commun.* **11**, 406 (2020).
- ²⁴J. Feldmann, M. Stegmaier, N. Gruhler, C. Rios, H. Bhaskaran, C. D. Wright, and W. H. P. Pernice, *Nat. Commun.* **8**, 1256 (2017).
- ²⁵C. M. Wu, H. S. Yu, S. Lee, R. M. Peng, I. Takeuchi, and M. Li, *Nat. Commun.* **12**, 96 (2021).
- ²⁶Y. F. Zhang, J. B. Chou, J. Y. Li, H. Li, Q. Y. Du, A. Yadav, S. Zhou, M. Y. Shalaginov, Z. R. Fang, H. K. Zhong, C. Roberts, P. Robinson, B. Bohlin, C. Rios, H. T. Lin, M. Kang, T. Gu, J. Warner, V. Liberman, K. Richardson, and J. J. Hu, *Nat. Commun.* **10**, 4279 (2019).
- ²⁷M. Delaney, I. Zeimpekis, D. Lawson, D. W. Hewak, and O. Muskens, *Adv. Funct. Mater.* **30**, 2002447 (2020).
- ²⁸M. Li, M. Z. Xie, H. Ji, J. Y. Zhou, K. Jiang, L. Y. Shang, Y. W. Li, Z. G. Hu, and J. H. Chu, *Appl. Phys. Lett.* **116**, 162102 (2020).
- ²⁹D. C. Sati, A. Kovalskiy, R. Golovchak, and H. Jain, *J. Non-Cryst. Solids* **358**, 163–167 (2012).
- ³⁰R. Golovchak, O. Shpotyuk, M. Iovu, A. Kovalskiy, and H. Jain, *J. Non-Cryst. Solids* **357**, 3454–3460 (2011).
- ³¹J. H. Warner, M. H. Rummeli, T. Gemming, B. Büchner, and G. A. D. Briggs, *Nano Lett.* **9**, 102–109 (2009).
- ³²J. K. Olson, H. Li, T. Ju, J. M. Viner, and P. C. Taylor, *J. Appl. Phys.* **99**, 103508 (2006).
- ³³W. M. J. Green, M. J. Rooks, L. Sekaric, and Y. A. Vlasov, *Opt. Express* **15**, 17106–17113 (2007).
- ³⁴C. Wang, M. Zhang, X. Chen, M. Bertrand, A. Shams-Ansari, S. Chandrasekhar, P. Winzer, and M. Lončar, *Nature* **562**, 101–104 (2018).
- ³⁵M. P. Singh, M. Mandal, K. Sethupathi, M. S. R. Rao, and P. K. Nayak, *Nanoscale Res. Lett.* **16**, 22 (2021).
- ³⁶S. Hwang, H. Park, D. Kim, H. Lim, C. Lee, J. H. Han, Y. K. Kwon, and M. H. Cho, *ACS Appl. Mater. Interfaces* **17**, 37285 (2020).
- ³⁷Y. Zhou, M. Y. Leng, Z. Xia, J. Zhong, H. B. Song, X. S. Liu, B. Yang, J. P. Zhang, J. Chen, K. H. Zhou, J. B. Han, Y. B. Cheng, and J. Tang, *Adv. Energy Mater.* **4**, 1301846 (2014).
- ³⁸M. Olivier, J. C. Tchahame, P. Nemeč, M. Chauvet, V. Besse, C. Cassagne, G. Boudebs, G. Renversez, R. Boidin, E. Baudet, and V. Nazabal, *Opt. Mater. Express* **4**, 525–540 (2014).
- ³⁹J. Feldmann, N. Youngblood, X. Li, C. D. Wright, H. Bhaskaran, and W. H. P. Pernice, *IEEE J. Sel. Top. Quantum Electron.* **26**, 1 (2020).